Superconducting $YBa_2Cu_3O_{7-\delta}$ nanocomposites using preformed ZrO_2 nanocrystals: Growth mechanisms and vortex pinning properties

Katrien De Keukeleere[1,2,▽], Pablo Cayado[3,▽], Alexander Meledin[4], Ferran Vallès[3], Jonathan De Roo[1,2], Hannes Rijckaert[1], Glenn Pollefeyt[1], Els Bruneel[1], Anna Palau[3], Mariona Coll[3], Susagna Ricart[3], Gustaaf Van Tendeloo[4], Teresa Puig[3], Xavier Obradors[3], and Isabel Van Driessche[1,]*

[1] Sol-Gel Centre for Research on Inorganic Powders and Thin Film Synthesis, SCRiPTS and [2] Physics and Chemistry of Nanostructures, PCN, Ghent University, Krijgslaan 281 S3, 9000 Gent, Belgium
[3] Institut de CieNCia de Materials de Barcelona, ICMAB – CSIC, Campus UA Barcelona, E-08193 Bellaterra, Catalonia, Spain
[4] Electron Microscopy for Materials Science, EMAT, University of Antwerp, Groenenborgerlaan 171 U430, 2020 Antwerpen, Belgium

[▽] Both authors contributed equally to this work.

*Corresponding author: Isabel.VanDriessche@ugent.be

Abstract. Although superconductors are promising for power applications, the production of low cost coated conductors with high current densities – in high magnetic fields – remains challenging. Via chemical solution deposition and in a reproducible manner, we fabricated a superior nanocomposite of preformed nanocrystals (NCs) in a superconducting coating, i.e., $YBa_2Cu_3O_{7-\delta}$. Preformed, colloidally stable ZrO_2 NCs were added to the trifluoroacetic acid based precursor solution. Dynamic light scattering confirmed the NCs' stability, even at high concentrations – up to 50 mol% – for at least 2.5 months. Interestingly, the NCs tend to disrupt the epitaxial growth of $YBa_2Cu_3O_{7-\delta}$, unless a thin seed layer is applied. The effect of different NC loadings in $YBa_2Cu_3O_{7-\delta}$ was investigated, and 10 mol-% ZrO_2 proved optimal, yielding a critical current density J_C of 5 MA/cm² at 77 K in self-field. Importantly, this new approach resulted in a smoother magnetic field dependency J_C(H//c) for the nanocomposite compared to a pristine film. Furthermore, microstructural analysis of the $YBa_2Cu_3O_{7-\delta}$ films revealed that different strain-coping mechanisms around the preformed nanocrystals occur, being either through the incorporation of stacking faults or by introducing heavily strained interfaces between the preformed NCs and the superconducting matrix. It is evidenced that the generated nanostrain in the NC-YBCO nanocomposite results in an improvement of the superconducting properties similar as for the spontaneous segregation approach previously reported.

Keywords. nanoparticles, TFA-YBCO, nanocomposites, chemical solution deposition

Introduction

Since the discovery of high-temperature superconductors (HTS), huge efforts have been dedicated to develop useful conductors for, e.g., power applications.[1-4] In this respect, low fabrication costs and high critical current densities in magnetic fields are required. Chemical solution deposition (CSD) is an appealing method towards the production of affordable, long length HTS tapes.[5-7] In this method, a precursor solution containing the metal salts is deposited on a metallic substrate (or single crystal on lab scale) and thermally treated to obtain the desired superconducting film. In particular, methanol-based solutions containing the trifluoroacetate salts of $YBa_2Cu_3O_{7-\delta}$ (YBCO) have been reported to yield epitaxial layers with high critical current densities (J_C = 2 – 4 MA/cm²).[8,9] However, these

epitaxial YBCO films still feature a strong J_C reduction with increasing magnetic fields, revealing new challenges for high field applications.[10] At a certain magnetic field value, small, non-superconducting regions appear surrounded by a paramagnetic vortex current. These vortices move throughout the superconductor under influence of the Lorentz force, causing a reduction in J_C. The vortices can be immobilized, or pinned, by the introduction of non-superconducting defects, so called artificial pinning centers (APCs), effectively decreasing the magnetic field dependence of J_C.[1,11-16]

Currently, CSD based YBCO films are improved by the spontaneous segregation or "in-situ" formation of secondary phases (APCs) in the YBCO matrix, a processing occurring during the formation of YBCO itself. Extra metal salts are added to the YBCO precursor solution to grow the desired secondary phase (e.g., Au, Y_2O_3, $BaZrO_3$, $BaCeO_3$, Ba_2YTaO_6).[11,17-23] Although this method yields effective, nanostructured superconducting layers, some limitations remain. Since this method relies on the spontaneous segregation of secondary phases, only limited control over the nanoparticles' formation is obtained and, as a consequence, the size and size distribution of the particles as well as the stoichiometric tuning of the inclusions is challenging.

A more interesting approach to improve the CSD based YBCO films is the addition of preformed nanocrystals (PNCs) to the YBCO precursor solution. This approach offers a better control of the APC size as non-aqueous synthesis methods, being surfactant-assisted or surfactant-free, can be used yielding monodisperse nanocrystals with different sizes and shapes.[24-29] So far, only a few reports, using preformed pinning centers have been reported in literature.[22,30,31] The first account was disclosed by Martinez-Julien *et al.* in 2011, who applied preformed Au nanocrystals (NCs).[22] In their approach, only a low amount of Au NCs (up to 2 mol-%) could be stabilized in the YBCO precursor. Unfortunately, the Au NCs were pushed to the YBCO surface during the treatment, unable to enhance vortex pinning. Bretos *et al.* described the introduction of amorphous $BaZrO_3$ nanoparticles in YBCO.[30] Yet, the improvement in critical current of the YBCO films was rather ascribed to an improved morphology of the sample than to the improvement of flux pinning provided by the $BaZrO_3$ nanoparticles. More recently, we described the introduction of preformed CeO_2 and ZrO_2 NCs to the YBCO film.[31] The CeO_2 NCs remain stable in the YBCO precursor up to a week at desirable concentrations (up to 32 mol-%). Interestingly, a difference in NC size (2 nm vs 6 nm) appeared to have an effect on the NC mobility during the thermal processing. The smaller NCs migrated to the film surface, while the larger ones were retained in the film itself. However, the J_c field dependence of the YBCO nanocomposite did not exceed the one of pristine YBCO. Preliminary results using preformed ZrO_2 NCs indicated that the PNCs settle at the substrate-YBCO interface, leading to poorly grown YBCO and deteriorating the superconducting properties.[31] However, the introduction of an interfacial YBCO seed layer in between the substrate and the YBCO nanocomposite can promote epitaxial YBCO growth.[31-33]

In this work, a comprehensive study was performed on the involved phenomena of the ZrO_2 NCs settling on the substrate and the influence of the use of a pure YBCO seed layer. First, the ZrO_2 NCs are synthesized via a microwave-assisted solvothermal treatment, yielding aggregated NCs of 7 nm directly after synthesis.[34,35] Through a post-synthetic surface treatment with hydrophobic ligands, the NCs become aggregate-free and are colloidally stable in apolar solvents. However, as the methanol-based YBCO precursor solution provides a polar environment, a ligand exchange is mandatory. This is not always straightforward, as the surface chemistry of metal oxide NCs is more complex compared to the surface chemistry of the more established chalcogenides.[36] The ZrO_2 PNCs can be stabilized in high concentration, up to 50 mol-%, for at least 2.5 months in a trifluoroacetic acid (TFA) YBCO precursor solution, by using the combination of a strong organic acid and an amino acid[37], confirmed

by dynamic light scattering analysis. Second, the YBCO-PNCs suspensions were deposited on a $LaAlO_3$ (LAO) substrate through spin-coating and subsequently treated at high temperatures to study the influence of the PNCs in the processed YBCO coating on the superconductor performance and its microstructure. XPS analysis and quench studies revealed that the PNCs already settle at the substrate interface during pyrolysis, before the YBCO growth. The use of a pure YBCO seed layer, on the other hand, indeed resulted in desirable YBCO growth. Here, an optimal critical current density J_C of 5 MA/cm^2 and an improved magnetic field dependency of J_C was found for the 10 mol-% PNC addition compared to pristine YBCO. Similar to the approach based on the spontaneous segregation of APCs, these PNC-YBCO nanocomposites show the generation of nanostrain in the YBCO matrix, either in the form of stacking faults or as highly strained PNC-YBCO interfaces, hereby leading to an effective pinning behavior at elevated magnetic fields.

Experimental

Nanocrystal synthesis. ZrO_2 NCs are synthesized according to a microwave-assisted solvothermal treatment.[34,38] The ZrO_2 NCs are synthesized using zirconium chloride and benzyl alcohol as solvent. After a microwave-assisted solvothermal treatment, a stable colloidal dispersion of the NCs capped with dodecanoic acid is obtained. To achieve a stable NC dispersion in methanol, a ligand exchange is performed. First, the dodecanoic acid-stabilized NCs are precipitated with acetone and subsequently glutamine (Gln), dissolved in dry methanol, is added together with trifluoroacetic anhydride (TFAA). An ultrasonic treatment of approximately 30 min results in a clear and colorless dispersion. The NCs suspension is purified by a precipitation-dissolution process using toluene to precipitate the NCs, and methanol to redisperse the purified NCs. More details can be found in the Supporting Information (S.I.).

Layer formation. YBCO – ZrO_2 precursor solutions are prepared by introducing the ZrO_2 NCs in different mol-% to a TFA-YBCO precursor solution. The preparation of the TFA-YBCO precursor solution is described elsewhere.[9] Mol-% of 0, 1, 3, 6, 10 and 15 % have been investigated. The YBCO – NCs precursor films are prepared by depositing the precursors on 5 mm x 5 mm $LaAlO_3$ (LAO) single crystal substrates via spin coating (6000 rpm for 2 min). These deposited layers are thermally treated for pyrolysis and subsequent crystallization to convert the layers into the final YBCO nanocomposite thin films.[8] Generally, the pyrolysis treatment was performed in a tubular furnace under a humid oxygen gas flow at 310 °C for 30 min. The crystallization treatment was performed at 810 °C for 180 min in a wet N_2 atmosphere with an O_2 partial pressure of 200 ppm. Finally, the superconducting YBCO phase was obtained by oxygen annealing at 450 °C for 210 min. To start from an LAO substrate with an interfacial pure YBCO seed layer, first a 0.375 M total metal concentration of TFA-YBCO precursor is deposited on the LAO substrate and spin-coated. This layer is pyrolyzed, without a dwell of 30 min, before the NCs-YBCO suspension is deposited on top. Directly afterwards, the bilayer is crystallized using the thermal treatment previously mentioned.

Nanocrystal characterization. The metal oxide NCs are characterized via transmission electron microscope (TEM) using a JEOL model JEM-2200FS, X-ray diffraction (XRD) using a Thermo Scientific ARL X'tra X-ray diffractometer with the Cu K_α line as primary X-ray source, and dynamic light scattering (DLS) measurements using a Malvern Nano ZS in backscattering mode (173°).

Layer characterization. The microstructure and phase analysis of the fully converted YBCO nanocomposite films was performed by two-dimensional (2D) X-ray diffraction (XRD) using a Bruker AXS GADDS diffractometer. The nanocrystal size,distribution, chemical composition and atomic scale

defects of the PNCs in the final nanocomposite layer was investigated via TEM as high resolution high angle annular dark field scanning transmission electron microscopy (HAADF-STEM) and energy dispersive X-ray spectroscopy (EDX) studies using a FEI Titan "cubed" electron microscope, equipped with an aberration corrector for the probe-forming lens as well as a high-brightness gun and a "Super-X" wide solid angle EDX detector. The electron microscope was operated at 200 kV acceleration voltage. X-ray photoelectron spectroscopy (XPS) measurements were recorded on a X-ray photoelectron spectroscopy S-Probe XPS spectrometer with monochromated Al (1486 eV) exciting radiation from Surface Science Instruments (VG). The flood gun was set at 3 eV. A nickel grid was placed 3 mm above the samples in order to suppress charging of the samples. The samples were attached to the stage using conducting C-tape, a shortcut between the top of the sample and the stage was prepared with Cu-tape. Experimental data were processed using the software package CasaXPS (Casa Software Ltd., UK), no calibration of peak positions was performed. Sputtering of an area of 3 × 3 mm^2 for 500 s/800 s was performed with an Ar^+ ion gun (4 keV) resulting in a sputter rate for Ta_2O_5 of 0.036 nm/s. After each consecutive sputter cycle an area of 250 × 1000 μm^2 was analysed. Regions for C 1s, Y 3d, Zr 3p-3p1/2, La 4p1/2, La3d5/2 and O 1s peaks were registered. Angular transport I(V) characteristics and resistivity measurements were carried out in a PPMS Quantum Design system provided with a 9 T magnet and variable temperature from 5 to 300 K. The superconducting transition temperature, T_c, the critical current density $J_C(T, H, \theta)$ and the irreversibility line $H_{irr}(T, \theta)$ were thus determined. Narrow bridges of 200 µm lengths and 10 to 30 µm width were fabricated with standard photolithography with a Durham Magneto Optics Std MicroWriter™. Silver metal contacts were evaporated and post-annealed, ensuring contact resistances below 10 $\mu\Omega$. Samples were measured with the standard four probe method. The applied current was sent parallel to the ab planes and J_c was determined by using a 10 μVcm^{-1} criterion. In angular measurements, the magnetic field was rotated from the *c*-axis (θ = 180°) to the *ab*-plane (θ = 90°), ensuring the maximum Lorentz force configuration.

Results & discussion

Nanocrystal stabilization

ZrO_2 NCs were synthesized from a microwave-assisted method, and have the monoclinic crystal phase according to XRD (Figure 1B). TEM analysis on the NCs after surface modification shows individual, elongated NCs with a long edge of about 7 nm (Figure 1 A). DLS analysis confirms the presence of individual, aggregate-free NCs in chloroform with an average solvodynamic diameter of 10 nm. As the solvodynamic diameter is defined as the sum of core and ligand in apolar solvents, the obtained value is in agreement with the size determined by TEM (Figure 1C). The transfer from chloroform to methanol with glutamine (Gln) and trifluoroacetic anhydride leads to a similar size distribution in DLS (Figure 1 C) confirming the success of the stabilization. In order to apply these NCs as pinning centers in superconductors, it is essential that the NCs remain stable in the highly ionic TFA-YBCO precursor solution. Different NC concentrations capped with Gln were introduced in a 0.75 M (total metal concentration) TFA-YBCO solution. DLS analyses on these suspensions show that even at high loadings, the colloidal integrity is maintained in this ionic environment (Figure 1 C). Moreover, these suspensions remain stable for at least 2.5 months, sufficient for usage as nanocomposite precursors. For the 50 mol-% NCs-YBCO suspension, some agglomeration starts to occur after 4 months, see Supporting Information (S.I.).

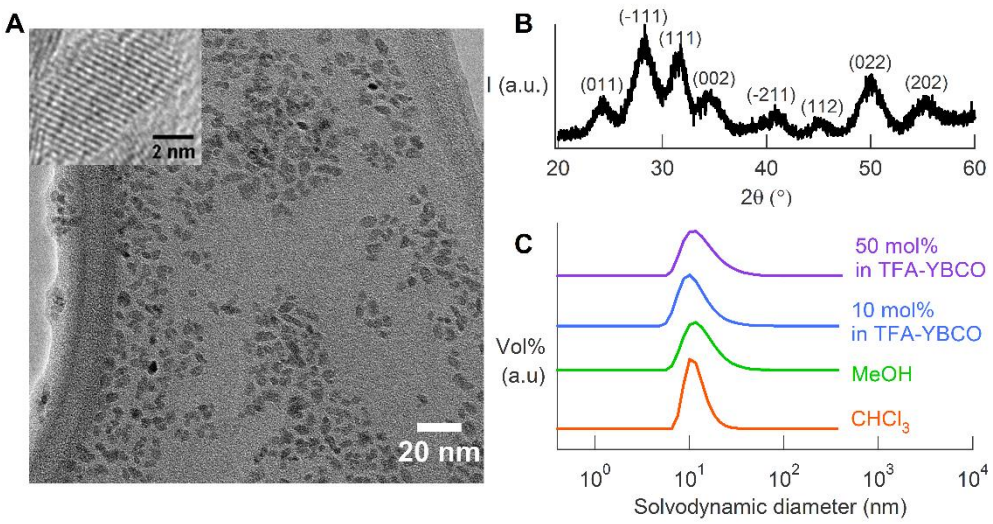

Figure 1. (A) Bright field and high resolution TEM and (B) XRD analysis of the monoclinic ZrO_2 NCs after synthesis and post-modification in chloroform. (C) DLS analysis of the ZrO2 NCs in chloroform, methanol, and 10 and 50 mol-% in TFA-YBCO precursor solution.

Layer formation

Preliminary results using preformed ZrO_2 NCs showed that high PNC loadings resulted in random and thus poorly grown YBCO, whereas the physical properties at lower amounts did not increase significantly.[31] Moreover, the initial ZrO_2 PNCs transformed to $BaZrO_3$ NCs during the crystallization treatment.[31] To assess when the PNCs settle at the substrate – during deposition, pyrolysis or crystallization – we performed a centrifugation experiment and XPS analyses, revealing that the ZrO_2 PNCs settle on the substrate during the pyrolysis treatment. Moreover, XRD experiments performed on quenched samples of the YBCO nanocomposite layers indicate that $BaZrO_3$, originating from the ZrO_2 PNCs, nucleates before YBCO formation. As the lattice mismatch between $BaZrO_3$ and YBCO is fairly high (i.e. 8 %), random *(103)* YBCO is formed when high amounts of the preformed ZrO_2 NCs are added. More detailed analysis is given in the Supporting Information (S.I.). Thus, settling of the NCs on at the substrate-YBCO interface should be avoided, to procure *c*-axis oriented YBCO growth. Settling of the NCs could for example be caused by the use of ligands stabilizing the NCs. If these ligands burn off too easily, the NCs will precipitate during the treatment before the layer is solidified. So, the use of more thermally stable ligands could lead to better YBCO layers. However, the ligand choice is restricted. Ligands containing a high content in metals, halides (except fluorine), sulfur or phosphor should be avoided, as these could otherwise negatively affect the final properties of the superconductor due to poisoning.[39] Moreover, NC stabilization in a highly ionic polar environment is not always straightforward.[37]

In order to promote *c*-axis oriented YBCO growth, we deposited a thin, pure YBCO seed layer in between the LAO substrate and the YBCO nanocomposite film. Nanocomposite films with different PNCs' amounts were tested, i.e. 0, 3, 6, 10 and 15 mol-% of preformed ZrO_2 NCs, deposited onto the YBCO seed layer. According to the XRD diffraction patterns displayed in Figure 2, all the nanocomposite films are *c*-axis oriented. The PNCs – YBCO nanocomposites show an additional 2θ reflection at 43° of *(200)* $BaZrO_3$ (BZO), and the 15 mol-% ZrO_2 NC addition reveals an extra reflection at 30° of *(110)* BZO, while ZrO_2 reflections remain absent. This suggests the complete transformation of the initial ZrO_2 NCs into BZO NCs during the heat treatment. All 2D X-ray diffraction patterns of the films containing the PNCs show epitaxial YBCO, while polycrystalline or random YBCO is absent. So

indeed, the presence of an interfacial YBCO layer has a beneficial effect on the PNCs – YBCO epitaxial growth.

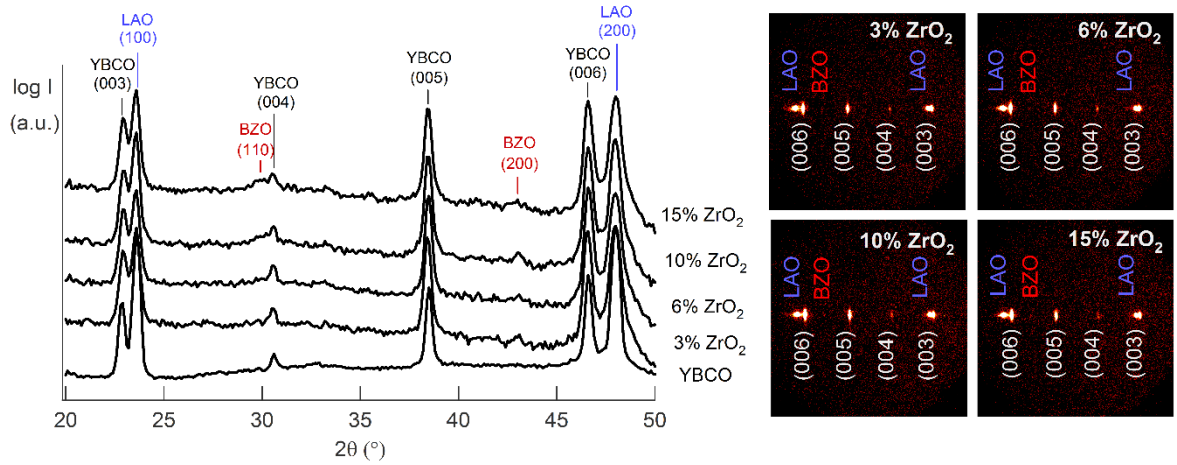

Figure 2. (2D-) XRD diffraction patterns of YBCO films with 0, 3, 6, 10 and 15 mol-% of preformed ZrO_2 NCs deposited on a LAO substrate with a 50 nm pure YBCO seed layer.

The size, distribution and local microstructure of the NCs in the YBCO layer were determined using HAADF-STEM and EDX. We investigated the nanocomposite films both after the pyrolysis and the crystallization treatment. As it becomes clear from the TEM and EDX images displayed in Figure 3A and B, the bottom 50 – 70 nm of the YBCO layer does not contain a Zr-rich phase, while the formed $BaZrO_3$ NCs are homogeneously distributed in the top YBCO layer. The individual NCs embedded in the layer coarsen from the initial 7 nm ZrO_2 NCs to 12 – 25 nm of $BaZrO_3$ NCs (Figure 3C), similarly to the case of "in-situ" nanocomposites, while some agglomeration of different initial NCs, is also clearly visible (Figure 3D). This agglomeration may already occur during the pyrolysis step, but it may also be induced during the crystallization process as a consequence of grain coalescence[40], a phenomenon also observed in "in-situ" nanocomposites[41].

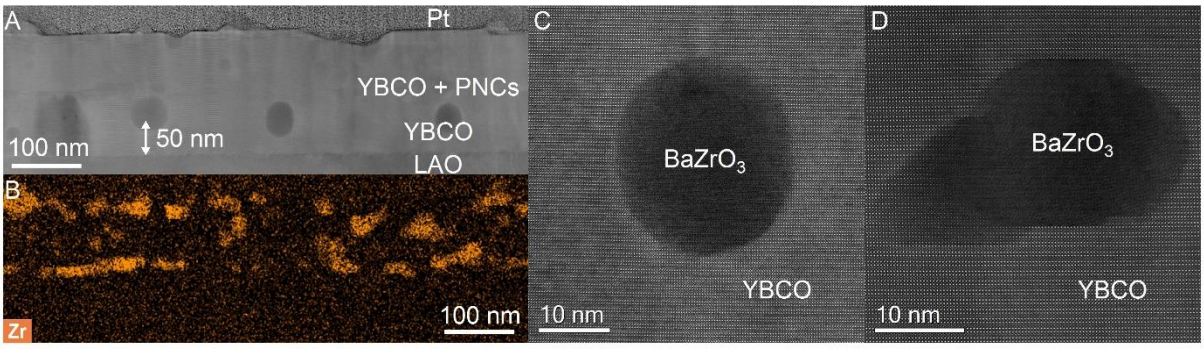

Figure 3. (A) HAADF-STEM cross sectional image and (B) EDX Zr map image of the 10 mol-% preformed PNCs-YBCO nanocomposite indicating the presence of Zr in the layer. (C-D) High-resolution HAADF-STEM Z-contrast image of the same nanocomposite showing local microstructures of $BaZrO_3$ NCs randomly oriented and sometimes faceted by YBCO *(001)* plane.

The elemental distribution in the pyrolyzed nanocomposite layer was also analyzed after the YBCO metal organic decomposition process. Figure 4 displays a HAADF image together with EDX images of all the elements included in the pyrolyzed nanocomposite. The HAADF image displays the typical porous structure of YBCO films after pyrolysis[8] while the EDX images clearly show that some element aggregation occurs. From this, it can be concluded that some ZrO_2 is accumulated at the interface between both YBCO layers, together with some CuO, while the ZrO_2 NCs are not transferred to the

YBCO seed layer. The CuO enrichment at the interface seems to arise from the upper layer, and so we can conclude that the CuO nanoparticles formed after the Cu-TFA pyrolysis (typically with a diameter of 10 nm) behave very efficiently as diffusion barrier for the preformed ZrO_2 NCs of the upper bilayer. The formation of enriched CuO layers at the interface of pyrolyzed films of TFA-YBCO precursors, after a multi-deposition process, has been previously reported.[12] Here, it was shown that these enriched CuO layers did not preclude the achievement of homogeneous YBCO films after crystallization. The enrichment of ZrO_2 NCs at the interface has been confirmed by XPS analysis (see Figure S??) from which it is clear that the effect is more prominent after the pyrolysis step than after the crystallization. So, the element distribution analysis clearly provides some hints on the advantages of using a bilayer structure to achieve superconducting films with high performance. Although a tendency to accumulate ZrO_2 NCs at the substrate interfaces exist during the pyrolysis, the use of an YBCO seed layer clearly hinders the diffusion of the PNCs to the LAO interface, and thus influences the YBCO epitaxial film nucleation process. As shown by XRD and TEM analysis, the monoclinic ZrO_2 NCs are recrystallized into perovskite BZO NCs. This recrystallization occurs through reaction with BaF_2 precursor, present during the thermal treatment. However, also YBCO nuclei are formed through the reaction with BaF_2, controlled by the wet atmosphere.[42,43] This means that competition between the crystallization kinetics of BZO and YBCO nuclei formation takes place at the interface, as a Zr-rich phase is already present at the interface after pyrolysis. The first BZO NCs are formed at the interface (heterogeneous nucleation) and these will be epitaxial.[11,44] Hence, the balance between the heterogeneous nucleation rates of BZO and YBCO will determine the final concentration of the BZO NCs at the interface. However, the YBCO homo-epitaxial nucleation rate will always be higher than the hetero-epitaxial one.[40,45] This means that the use of a bilayer structure will promote a faster formation of YBCO nuclei and a reduced concentration of BZO NCs at the interface, as it is indeed experimentally confirmed and thus the epitaxial quality of the YBCO-BZO nanocomposite films is enhanced in the bilayer structure.

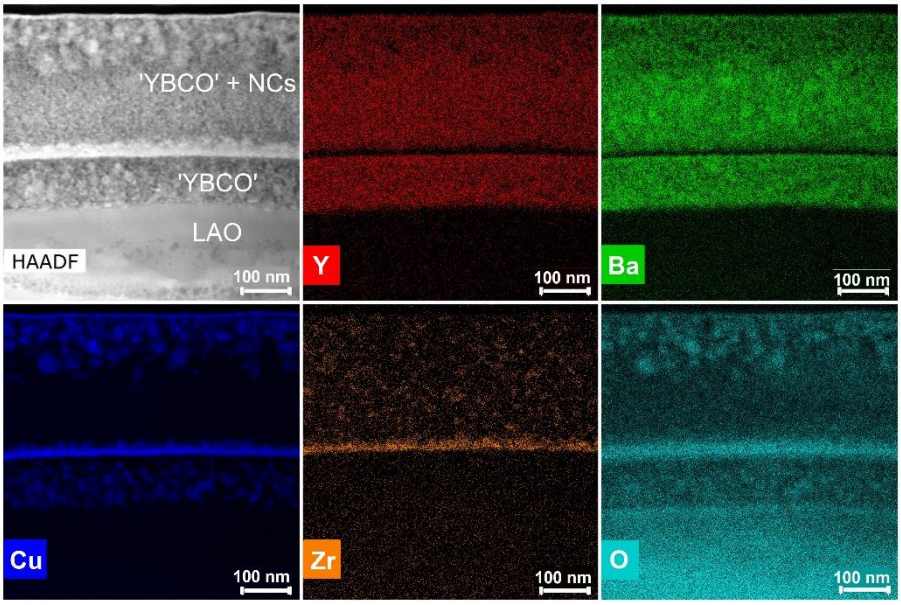

Figure 4. HAADF-STEM cross sectional image and EDX imaging of Y, Ba, Cu, Zr and O obtained after the pyrolysis treatment of a 15 mol-% PNCs – YBCO nanocomposite containing a pure YBCO seed layer.

Another remarkable feature of the present YBCO-BZO nanocomposites concerns the issue of the defect structure induced by the NCs. As commonly seen in nanocomposites formed via the

spontaneous segregation approach, the introduction of nano-sized secondary phases induces stacking faults (double or triple CuO chain layers) and hereby leads to a heavily strained YBCO matrix at the nanoscale. It has been proposed that this nanostrain can be correlated to the effective pinning properties and it is therefore believed to be essential in order to obtain enhanced in-field behavior of the superconducting architecture.[20,25,34] In the present case, similar as for the spontaneous segregation approach, the BZO nanocrystals are not biaxially textured within the matrix, which mostly leads to the formation of incoherent interfaces. However, as could already be seen in high resolution HAADF-STEM images in Figure 3, the incorporation of BZO nanocrystals in the YBCO matrix is also possible without the formation of these stacking faults. Nevertheless, the YBCO surrounding the nanocrystals is clearly strained at the nanocrystal-YBCO interface, as shown by the bright contrast surrounding the nanocrystals in the LAADF-STEM images given in Figure 5. Next to this, also regions showing short stacking faults in close proximity of the BZO nanocrystals can be observed, as specified by the white arrows in Figure 5B. Nevertheless, this indicates that the different approaches, PNCs versus spontaneous segregation, can lead to different growth features, either due to modified kinetics or due to the modified interface energy, which may also influence the defect generation pattern and thus affect the YBCO's microstructure. $BaZrO_3$ NCs, via spontaneous segregation, are formed (nucleation and growth) under the same growth conditions as YBCO[11], while the recrystallized BZO NCs formed in the present case probably arise through some case of topotactical reaction of ZrO_2 with Ba^{2+} ions and thus probably have a modified surface structure. We note, for instance, that some of the BZO NCs embedded in the YBCO matrix display facets parallel to CuO_2 planes of YBCO (Figure 3D), probably indicating that a dense plane is formed and hence the NCs have some local uniaxial texture. Additionally, the possible incorporation of small amounts of Y^{3+} into the $BaZrO_3$ crystal structure could also induce structural or chemical changes at the nanocrystal's surface. A modified interface structure can certainly cause a modified growth process of YBCO films, which in some cases may lead to a decrease or even an elimination of the defect generation capability at the non-coherent interface, and so a modified nanostrain distribution may arise, including heavily strained interfaces as shown in Figure 5C. According to X-ray diffraction experiments performed on quenched samples of the PNC – YBCO layers (see S.I.), it is very likely that the homogeneously nucleated $BaZrO_3$ NCs, originating from the ZrO_2 PNCs, are formed before the full YBCO film is grown, similarly to the case of "in-situ" nanocomposites (i.e. via spontaneous segregation). We should note that the final values of YBCO films nanostrain, as determined through X-ray diffraction, appear similar in both cases reaching a maximum nanostrain ε of 0.24% for the 10 mol-% NC in comparison with a nanostrain ε of 1% for the pristine sample.[32,44]

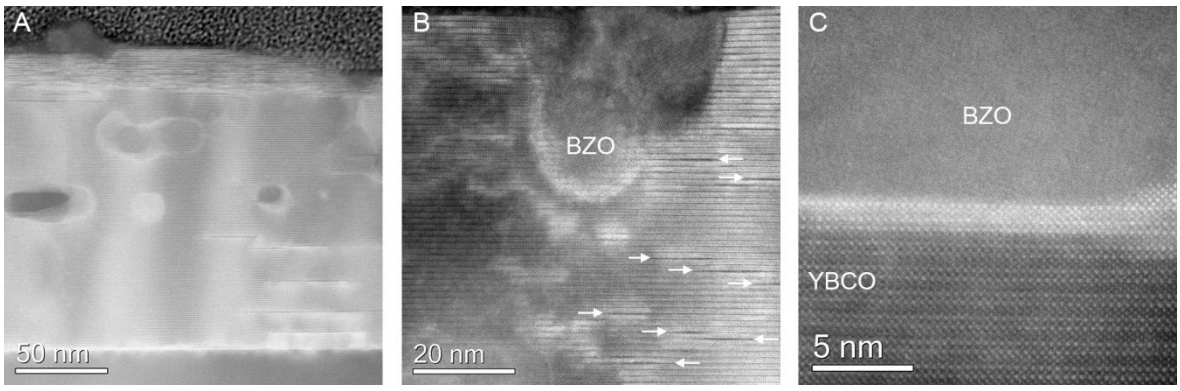

Figure 5. (A) LAADF-STEM cross sectional image showing the nanocrystal distribution and the presence of CuO stacking faults in the 10 mol-% PNCs – YBCO nanocomposite (B-C) High-resolution LAADF-STEM image of the same nanocomposite

showing local microstructures of BZO NCs, indicating highly strained BZO/YBCO interfaces (bright contrast) and short CuO stacking faults (indicated by white arrows).

Superconducting properties

The investigation of the superconducting properties demonstrated the successfulness of our PNC approach to enhance vortex pinning. Figure 6A represents the magnetic field dependence of the transport critical current, $J_C(H//c)$, at 77 K for the 6, 10 and 15 mol-% ZrO_2 nanocomposites and a pristine YBCO film. All the samples show high self-field critical current densities, from $J_c^{sf} \sim 2$ to 5 MA/cm^2. In the case of the nanocomposite with 15 mol-% ZrO_2, the reduction of J_c^{sf} could be ascribed to a reduction of the effective cross section due to a plausible agglomeration of NCs, as observed in CSD nanocomposites for high nanoparticles concentrations.[17] For the 10 mol-% ZrO_2 nanocomposite, an overall increase of J_C occurs at 77 K up to 5 T, whereas above this 5 T, J_C decreases below the pristine film suggesting a decrease of the irreversibility line (IL) (*vide infra*). Overall, we observe a smoother $J_C(H)$ behaviour for all nanocomposites marked with an extended $J_C(H)$ plateau, i.e. a shift of H* to higher fields from 0.03 T to 0.08 T (see inset Figure 6A). Being H* the crossover magnetic field from a single vortex pinning to a vortex-vortex collective pinning regime, it confirms that the amount of artificial pinning centre sites has strongly increased in all nanocomposites.

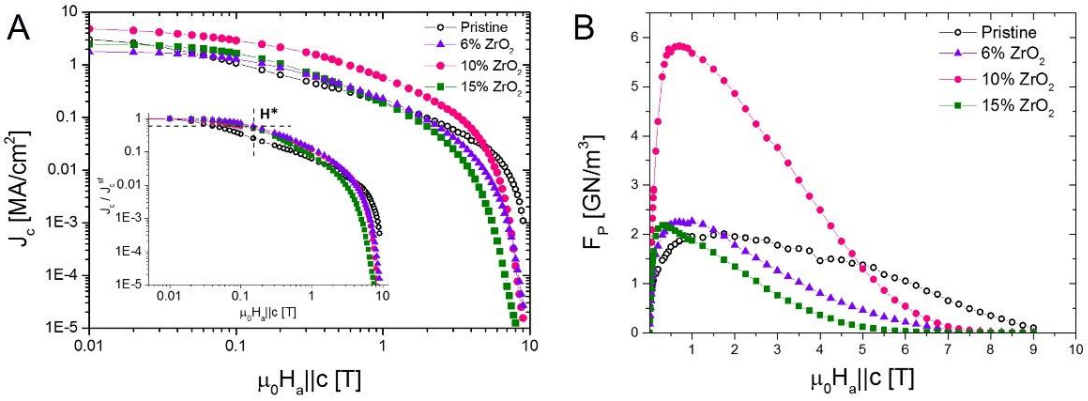

Figure 6. (A) Critical current density vs magnetic field at 77 K for YBCO samples with different NC content and a pristine film. The inset shows the same curves normalized to J_c^{sf}, where the H* value obtained for the nanocomposites is indicated. (B) Magnetic field dependence of the pinning force at 77 K for a pristine YBCO film and YBCO nanocomposite films containing different NC amounts.

The addition of PNCs does not decrease the critical temperature T_C, although the transition width (ΔT) rises drastically to 5.4 K when 15 mol-% PNCs are added to the YBCO layer in comparison with the ΔT = 1.5 K of the 6 mol-% NC, again implying that higher mol-% lead to a degradation of the superconductor. Figure 6B shows the pinning force, F_p, as a function of magnetic field for the 3 nanocomposites in comparison with the pristine film. Notice that F_p increases up to 6 GN/m^3 for the 10 mol-% ZrO_2, being 3 times larger than the pristine film, although a clear enhancement is not observed for the other two nanocomposites. This clearly indicates that an optimum amount of NCs exists for this growth process which is around 10 mol-% PNC. This value is still much lower than the best values reported from $BaZrO_3$ NCs formed via spontaneous segregation (10 - 22 GN/m^3)[11], which encourage us that further optimization is possible in this new approach. We also notice that the maximum pinning force is reached at lower magnetic fields (~ 0.5T - 0.8T) in all the nanocomposites compared to the pristine sample, again probably as a consequence of their lower IL. Therefore, we envisage that much higher pinning forces could be obtained upon optimization of the IL.

From the angular dependence transport critical current measurements (Figure 7A), we observe a similar behavior as for the spontaneous segregated nanocomposite approach. The broadening of the peak at H//ab (θ = 90°) is typically attributed to the effective pinning of the stacking faults present in the CSD nanocomposite[46]. Additionally, the peak at H//c, is clearly reduced for the nanocomposite. This peak is typically correlated to twin boundary pinning. As this peak can be observed in the pristine YBCO film, the reduction in the nanocomposite indicates a loss of the twin boundary coherence along the *c*-axis, as previously reported.[47,48] Clearly, the $J_C(H//ab)$ peak is much wider for the nanocomposite film compared to the pristine film at all magnetic fields (see Figure 7 at 65 K). The determination of the FWHM of this peak, $\Delta\theta$, for all nanocomposites at 1 T, 5 T and 9 T at 65 K is shown in Figure 7B. This clearly confirms that the ab peak broadens in all the nanocomposites, while a maximum effect for the one with 10 mol-% ZrO_2 NC addition is observed. This demonstrates the effective stacking fault pinning in all the nanocomposites with maximum effectiveness for samples with 10 mol-% NCs.

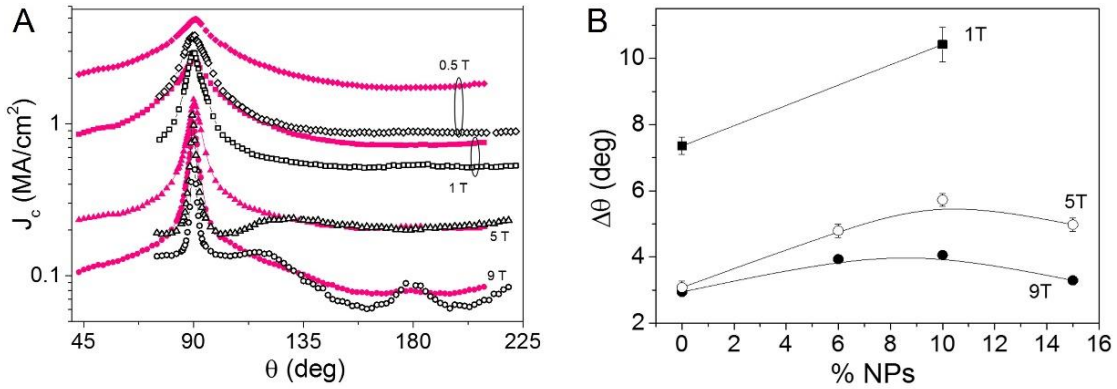

Figure 7. (A) Angular dependence of the critical current density, obtained at 65 K and different magnetic fields, for a pristine sample (open symbols) and a nanocomposite with 10 mol-% ZrO_2 (closed symbols). (B) FWHM of of the H//ab peak vs nanocrystal content obtained at 65 K for different magnetic fields.

Finally, Figure 8A shows the IL for a pristine YBCO film compared to YBCO nanocomposites films. Here, we confirm that the nanocomposites show a lower IL, which we ascribe to a lower *c*-axis correlation of twin boundaries due to the presence of stacking faults.[47,48] This reduction is more evident in the nanocomposite with a larger NC content. A thorough analysis of the angular dependence of the IL has enabled us to determine the effective anisotropy, γ_{eff}, for these PNCs-YBCO nanocomposites and confirm that the γ_{eff} is reduced from $\gamma_{eff} \sim 5$ to $\gamma_{eff} \sim 3$ by increasing the PNC content from 6 to 15 mol-% (see Figure 8B), which is similar to the values reported for spontaneously segregated CSD nanocomposites.[32] This suggests that the vortex pinning properties encountered in the PNC-YBCO nanocomposites have a similar origin than the ones reported for spontaneously segregated NCs. The present state of this new approach is still in its infancy and its potentiality might be enormous if we can avoid reactivity and coarsening of the preformed nanoparticles.

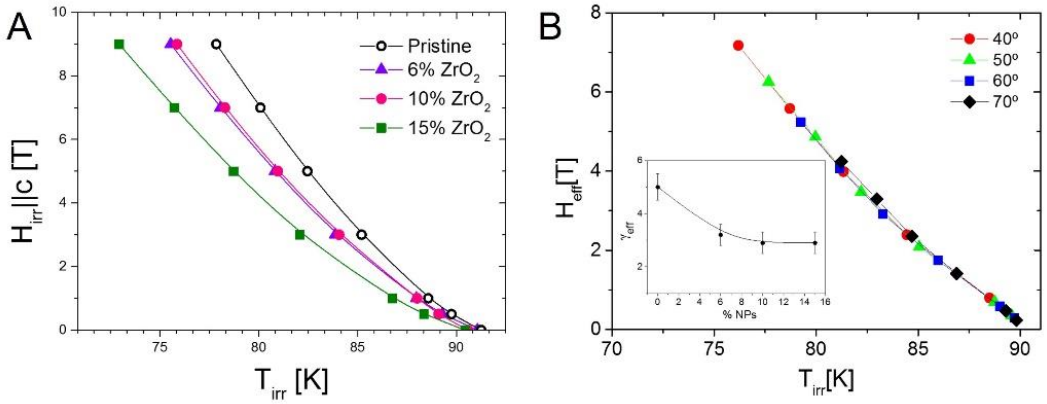

Figure 8. (A) Irreversibility lines (ILs) measured for YBCO samples with different nanocrystal content and a pristine film. (B) Isotropic collapse of the IL curves obtained, following the Blatter scaling approach with γ_{eff} = 2.9, for the 10 mol-% ZrO_2 nanocomposite. Inset shows the effective anisotropy value as a function of the nanoparticle content.

Conclusions

We presented a new, successful method to incorporate pinning centers in a high-temperature superconductor through the addition of preformed nanocrystals (PNCs) using a CSD approach.

First, we demonstrate the stability of the synthesized ZrO_2 nanocrystals, of only 7 nm, in a TFA-YBCO precursor solution. These as-synthesized nanocrystals are initially capped with long chain fatty acids, ensuring colloidal stability in nonpolar solvents. However, as the YBCO precursor typically provides a more polar environment, e.g., methanol, a ligand exchange with glutamine and trifluoroacetic anhydride was performed. Moreover, we are able to stabilize the PNCs up to 50 mol-% for at least 2.5 months in a TFA-YBCO precursor solution.

Second, different YBCO-PNCs suspensions were deposited on a $LaAlO_3$ substrate through spin-coating to study the influence of the PNCs in the YBCO coating. The PNCs settle at the substrate-YBCO interface during the pyrolysis treatment, leading an unacceptable growth of the final YBCO film and subsequent decrease in critical current density compared to the pristine YBCO films. However, by using a pure YBCO seed layer in between the $LaAlO_3$ substrate and the PNCs-YBCO nanocomposite film, an optimal critical current density J_C of 5 MA/cm² at 77 K in self-field could be obtained for a 10 mol-% PNCs addition. Furthermore, a smoother magnetic field dependence J_C(H//c) and a pinning force increase by a factor 3 at high magnetic fields was observed opening the field for this new approach. Analysis of the angular dependent critical current density and irreversibility line evidence that similar vortex pinning mechanisms account for the effective increase of the superconducting properties of the PNC-YBCO nanocomposites than for the self-segregated CSD nanocomposites approach previously reported.

This new, successful approach of incorporation of PNCs in CSD coatings holds the promise to the effective and economically efficient application of high-temperature superconductors in high and alternating magnetic field applications, relevant in alternative energy generation.

Acknowledgements

This work was financially supported by a BOF research fund of Ghent University (BOF11/DOC/286), FWO Flanders (F08512), and Eurotapes, a collaborative project funded by the European Community's Seven Framework Program (EU-FP7 NMP-LA-2012-280432). We also acknowledge MINECO and

FEDER funds for MAT2014-51778-C2-1-R and the Center of Excellence award Severo Ochoa SEV-2015-0496, and SGR753 from the Generalitat of Catalunya.

References

(1) Larbalestier, D.; Gurevich, A.; Feldmann, D. M.; Polyanskii, A. *Nature* **2001**, *414*, 368.

(2) Malozemoff, A. P. In *Annual Review of Materials Research, Vol 42*; Clarke, D. R., Ed.; Annual Reviews: Palo Alto, 2012; Vol. 42, p 373.

(3) Obradors, X.; Puig, T. *Supercond. Sci. Technol.* **2014**, *27*, 17.

(4) Shiohara, Y.; Taneda, T.; Yoshizumi, M. *Jpn. J. Appl. Phys.* **2012**, *51*, 16.

(5) Araki, T.; Hirabayashi, I. *Supercond. Sci. Technol.* **2003**, *16*, R71.

(6) Obradors, X.; Puig, T.; Ricart, S.; Coll, M.; Gazquez, J.; Palau, A.; Granados, X. *Supercond. Sci. Technol.* **2012**, *25*.

(7) Van Driessche, I.; Feys, J.; Hopkins, S. C.; Lommens, P.; Granados, X.; Glowacki, B. A.; Ricart, S.; Holzapfel, B.; Vilardell, M.; Kirchner, A.; Backer, M. *Supercond. Sci. Technol.* **2012**, *25*.

(8) Llordes, A.; Zalamova, K.; Ricart, S.; Palau, A.; Pomar, A.; Puig, T.; Hardy, A.; Van Bael, M. K.; Obradors, X. *Chem. Mat.* **2010**, *22*, 1686.

(9) Roma, N.; Morlens, S.; Ricart, S.; Zalamova, K.; Moreto, J. M.; Pomar, A.; Puig, T.; Obradors, X. *Supercond. Sci. Technol.* **2006**, *19*, 521.

(10) Obradors, X.; Puig, T.; Palau, A.; Pomar, A.; Sandiumenge, F.; Mele, P.; Matsumoto, K. In *Comprehensive Nanoscience and Technology*; Editors-in-Chief: David, L. A., Gregory, D. S., Gary, P. W., Eds.; Academic Press: Amsterdam, 2011, p 303.

(11) Gutierrez, J.; Llordes, A.; Gazquez, J.; Gibert, M.; Roma, N.; Ricart, S.; Pomar, A.; Sandiumenge, F.; Mestres, N.; Puig, T.; Obradors, X. *Nat. Mater.* **2007**, *6*, 367.

(12) Holesinger, T. G.; Civale, L.; Maiorov, B.; Feldmann, D. M.; Coulter, J. Y.; Miller, J.; Maroni, V. A.; Chen, Z. J.; Larbalestier, D. C.; Feenstra, R.; Li, X. P.; Huang, M. B.; Kodenkandath, T.; Zhang, W.; Rupich, M. W.; Malozemoff, A. P. *Adv. Mater.* **2008**, *20*, 391.

(13) Kang, S.; Goyal, A.; Li, J.; Gapud, A. A.; Martin, P. M.; Heatherly, L.; Thompson, J. R.; Christen, D. K.; List, F. A.; Paranthaman, M.; Lee, D. F. *Science* **2006**, *311*, 1911.

(14) Macmanus-Driscoll, J. L.; Foltyn, S. R.; Jia, Q. X.; Wang, H.; Serquis, A.; Civale, L.; Maiorov, B.; Hawley, M. E.; Maley, M. P.; Peterson, D. E. *Nat. Mater.* **2004**, *3*, 439.

(15) Matsumoto, K.; Mele, P. *Supercond. Sci. Technol.* **2010**, *23*, 014001.

(16) Xu, A.; Delgado, L.; Khatri, N.; Liu, Y.; Selvamanickam, V.; Abraimov, D.; Jaroszynski, J.; Kametani, F.; Larbalestier, D. C. *APL Mater.* **2014**, *2*, 8.

(17) Coll, M.; Guzman, R.; Garces, P.; Gazquez, J.; Rouco, V.; Palau, A.; Ye, S.; Magen, C.; Suo, H.; Castro, H.; Puig, T.; Obradors, X. *Supercond. Sci. Technol.* **2014**, *27*, 9.

(18) Ding, F. Z.; Gu, H. W.; Zhang, T.; Wang, H. Y.; Qu, F.; Peng, X. Y.; Zhou, W. W. *Acta Phys. Sin.* **2013**, *62*.

(19) Ding, F. Z.; Gu, H. W.; Zhang, T.; Wang, H. Y.; Qu, F.; Qiu, Q. Q.; Dai, S. T.; Peng, X. Y. *Chin. Phys. B* **2013**, *22*.

(20) Ding, F. Z.; Gu, H. W.; Zhang, T.; Wang, H. Y.; Qu, F.; Qiu, Q. Q.; Dai, S. T.; Peng, X. Y.; Cao, J. L. *Appl. Surf. Sci.* **2014**, *314*, 622.

(21) Jin, L. H.; Zhang, S. N.; Yu, Z. M.; Li, C. S.; Feng, J. Q.; Sulpice, A.; Wang, Y.; Zhang, P. X. *Mater. Chem. Phys.* **2015**, *149*, 188.

(22) Martinez-Julian, F.; Ricart, S.; Pomar, A.; Coll, M.; Abelian, P.; Sandiumenge, F.; Casanove, M. J.; Obradors, X.; Puig, T.; Pastoriza-Santos, I.; Liz-Marzan, L. M. *J. Nanosci. Nanotechnol.* **2011**, *11*, 3245.

(23) Petrisor, T.; Mos, R. B.; Nasui, M.; Gabor, M. S.; Augieri, A.; Celentano, G.; De Felkis, D.; Bemporad, E.; Ciontea, L. *J. Supercond. Nov. Magn* **2014**, *27*, 2493.

(24) Baghbanzadeh, M.; Carbone, L.; Cozzoli, P. D.; Kappe, C. O. *Angew. Chem.-Int. Edit.* **2011**, *50*, 11312.

(25) Jun, Y. W.; Choi, J. S.; Cheon, J. *Angew. Chem.-Int. Edit.* **2006**, *45*, 3414.

(26) Lee, J.; Zhang, S.; Sun, S. H. *Chem. Mat.* **2013**, *25*, 1293.

(27) Park, J.; Joo, J.; Kwon, S. G.; Jang, Y.; Hyeon, T. *Angew. Chem.-Int. Edit.* **2007**, *46*, 4630.

(28) Pinna, N.; Niederberger, M. *Angew. Chem.-Int. Edit.* **2008**, *47*, 5292.

(29) Shi, S.; Hwang, J.-Y. *Journal of Minerals & Materials Characterization & Engineering* **2003**, *2*, 101.

(30) Bretos, I.; Schneller, T.; Falter, M.; Backer, M.; Hollmann, E.; Wordenweber, R.; Molina-Luna, L.; Van Tendeloo, G.; Eibl, O. *J. Mater. Chem. C* **2015**, *3*, 3971.

(31) Cayado, P.; De Keukeleere, K.; Garzon, A.; Perez-Mirabet, L.; Meledin, A.; De Roo, J.; Valles, F.; Mundet, B.; Rijckaert, H.; Pollefeyt, G.; Coll, M.; Ricart, S.; Palau, A.; Gazquez, J.; Ros, J.; Van Tendeloo, G.; Van Driessche, I.; Puig, T.; Obradors, X. *Supercond. Sci. Technol.* **2015**, *28*, 18.

(32) Llordes, A.; Palau, A.; Gazquez, J.; Coll, M.; Vlad, R.; Pomar, A.; Arbiol, J.; Guzman, R.; Ye, S.; Rouco, V.; Sandiumenge, F.; Ricart, S.; Puig, T.; Varela, M.; Chateigner, D.; Vanacken, J.; Gutierrez, J.; Moshchalkov, V.; Deutscher, G.; Magen, C.; Obradors, X. *Nat. Mater.* **2012**, *11*, 329.

(33) Palau, A.; Puig, T.; Obradors, X.; Pardo, E.; Navau, C.; Sanchez, A.; Usoskin, A.; Freyhardt, H. C.; Fernandez, L.; Holzapfel, B.; Feenstra, R. *Appl. Phys. Lett.* **2004**, *84*, 230.

(34) De Keukeleere, K.; De Roo, J.; Lommens, P.; Martins, J. C.; Van der Voort, P.; Van Driessche, I. *Inorganic Chemistry* **2015**, *54*, 3469.

(35) De Roo, J.; De Keukeleere, K.; Feys, J.; Lommens, P.; Hens, Z.; Van Driessche, I. *J. Nanopart. Res.* **2013**, *15*, 1778.

(36) De Roo, J.; Justo, Y.; De Keukeleere, K.; Van den Broeck, F.; Martins, J. C.; Van Driessche, I.; Hens, Z. *Angew. Chem.-Int. Edit.* **2015**, *54*, 1.

(37) De Roo, J.; Coucke, S.; Rijckaert, H.; De Keukeleere, K.; Sinnaeve, D.; Hens, Z.; Martins, J. C.; Van Driessche, I. *Langmuir* **2016**, *Accepted*.

(38) De Roo, J.; Van den Broeck, F.; De Keukeleere, K.; Martins, J. C.; Van Driessche, I.; Hens, Z. *Journal of the American Chemical Society* **2014**, *136*, 9650.

(39) Foltyn, S. R.; Civale, L.; Macmanus-Driscoll, J. L.; Jia, Q. X.; Maiorov, B.; Wang, H.; Maley, M. *Nat. Mater.* **2007**, *6*, 631.

(40) Obradors, X.; Puig, T.; Gibert, M.; Queralto, A.; Zabaleta, J.; Mestres, N. *Chemical Society Reviews* **2014**, *43*, 2200.

(41) Coll, M.; Guzman, R.; Garces, P.; Gazquez, J.; Rouco, V.; Palau, A.; Ye, S.; Magen, C.; Suo, H.; Castro, H.; Puig, T.; Obradors, X. *Supercond. Sci. Technol.* **2014**, *27*.

(42) Obradors, X.; Puig, T.; Pomar, A.; Sandiumenge, F.; Mestres, N.; Coll, M.; Cavallaro, A.; Roma, N.; Gazquez, J.; Gonzalez, J. C.; Castano, O.; Gutierrez, J.; Palau, A.; Zalamova, K.; Morlens, S.; Hassini, A.; Gibert, M.; Ricart, S.; Moreto, J. M.; Pinol, S.; Isfort, D.; Bock, J. *Supercond. Sci. Technol.* **2006**, *19*, S13.

(43) Obradors, X.; Puig, T.; Ricart, S.; Coll, M.; Gazquez, J.; Palau, A.; Granados, X. *Supercond. Sci. Technol.* **2012**, *25*, 123001.

(44) Palau, A.; Llordes, A.; Gibert, M.; Puig, T.; Pomar, A.; Obradors, X. *IEEE Trans. Appl. Supercond.* **2011**, *21*, 3243.

(45) Obradors, X.; Martinez-Julian, F.; Zalamova, K.; Vlad, V. R.; Pomar, A.; Palau, A.; Llordes, A.; Chen, H.; Coll, M.; Ricart, S.; Mestres, N.; Granados, X.; Puig, T.; Rikel, M. *Physica C-Superconductivity and Its Applications* **2012**, *482*, 58.

(46) Palau, A.; Bartolome, E.; Llordes, A.; Puig, T.; Obradors, X. *Supercond. Sci. Technol.* **2011**, *24*.

(47) Guzman, R.; Gazquez, J.; Rouco, V.; Palau, A.; Magen, C.; Varela, M.; Arbiol, J.; Obradors, X.; Puig, T. *Appl. Phys. Lett.* **2013**, *102*, 5.

(48) Rouco, V.; Palau, A.; Guzman, R.; Gazquez, J.; Coll, M.; Obradors, X.; Puig, T. *Supercond. Sci. Technol.* **2014**, *27*, 7.